

The Dynamical Influence of Separate Teleconnections from the Pacific and Indian Oceans on the Northern Annular Mode

CHRISTOPHER G. FLETCHER

University of Waterloo, Waterloo, Ontario, Canada

CHRISTOPHE CASSOU

CNRS-CERFACS, Toulouse, France

(Manuscript received 8 December 2014, in final form 24 June 2015)

ABSTRACT

The northern annular mode (NAM) influences wintertime climate variability in the Northern Hemisphere, and understanding the processes controlling its sign and amplitude is of critical importance. Mounting evidence supports a robust teleconnection between the El Niño–Southern Oscillation (ENSO) and the NAM, while internal variability generated in the tropical Indian Ocean (TIO) may be associated with a NAM response of the opposite sign. This study uses a coupled ocean–atmosphere model to separate the influence on the NAM from teleconnections driven by ENSO and the TIO. In composites constructed using a long pre-industrial control integration, increased December–February precipitation in the central/eastern Pacific drives a negative late-winter NAM response. When isolated from ENSO variability, increased precipitation over the western-central TIO drives a strong and persistent positive NAM response throughout the winter. Opposite linear interference of the anomalous wave teleconnections explains most of the opposite-signed planetary wavelike driving of the NAM responses. The case with combined ENSO and TIO variability yields cancellation of the wave interference and a weak NAM response. This mechanism is confirmed using experiments where the tropical ocean is nudged separately over the Pacific and TIO to the large-amplitude 1997/98–1998/99 ENSO cycle. The phases of the Rossby wave and NAM responses in these two cases are of opposite sign, providing strong evidence that internal variability over the TIO can induce teleconnections independent of—and with opposite sign to—those associated with ENSO.

1. Introduction

There is a growing consensus that the El Niño–Southern Oscillation (ENSO) impacts wintertime extratropical climate through modulations to the northern annular mode (NAM), with warming in the tropical Pacific Ocean associated with the negative phase of NAM (e.g., Brönnimann 2007). Yet other regions of the tropical oceans warm concurrently during ENSO events, notably the tropical Indian Ocean (TIO; see Table 1 for a full list of acronyms; Trenberth et al. 2002), which

is a region that has also been linked with teleconnections to the northern extratropics (Hoerling et al. 2004; Bader and Latif 2005; Annamalai et al. 2007; Fletcher and Kushner 2013, hereafter FK13, 2011, hereafter FK11). Previous work using idealized modeling [with specified sea surface temperature (SST)] has shown that warm anomalies in the tropical east Pacific (TEP) and TIO can produce opposite-signed responses in extratropical temperature and precipitation (Barsugli and Sardeshmukh 2002) and in the phase of the NAM (FK13, FK11). If this effect is present in nature, then it implies that ENSO–NAM teleconnections may be modulated by SST anomalies and associated diabatic heating outside of the TEP, particularly from the TIO, that occurs most often in conjunction with ENSO events.

The SSTs in the TIO have exhibited a monotonic warming trend since 1950 (Hoerling et al. 2004), which implies that the character of ENSO–NAM teleconnections may be nonstationary. In addition to considerable internal

 Denotes Open Access content.

Corresponding author address: Christopher G. Fletcher, Department of Geography and Environmental Management, University of Waterloo, 200 University Ave. West, Waterloo ON N2L 3G1, Canada.
E-mail: chris.fletcher@uwaterloo.ca

DOI: 10.1175/JCLI-D-14-00839.1

TABLE 1. Definition of acronyms and study regions used in this study.

Acronym	Full name	Regional boundaries
TIO	Tropical Indian Ocean	30°S–10°N, 40°–120°E
TEP	Tropical east Pacific	10°S–10°N, 180°–90°W
TWP	Tropical west Pacific	10°S–10°N, 120°E–180°
P _a I _a	piControl composite with same-signed warm/cool TEP and TIO	—
P _a I _n	piControl composite with warm/cool TEP and neutral TIO	—
P _n I _a	piControl composite with neutral TEP and same-signed warm/cool TIO	—
NUD _{PAC}	Nudging experiment (TEP)	—
NUD _{IND}	Nudging experiment (TIO)	—

variability and a small sample size of large ENSO events, this may provide a partial explanation for why ENSO–NAM teleconnections have been reported in many (mostly idealized) modeling studies (Bell et al. 2009; Ineson and Scaife 2009; Cagnazzo and Manzini 2009; Randel et al. 2009; Taguchi and Hartmann 2006; Garfinkel and Hartmann 2008) but are either absent, or not statistically significant, in observation-based data (Randel et al. 2009; Free and Seidel 2009). One recent exception is the work of Butler et al. (2014), who show that ENSO–NAM teleconnections of the expected sign do emerge in reanalysis data, but mainly in cases that involve sudden stratospheric warming (SSW) events. They show that the subseasonal climate response in ENSO winters with/without SSWs is similar over North America but roughly opposite over Eurasia. These results, and the earlier modeling study by Bell et al. (2009), support the idea that a so-called stratospheric pathway is required to transform ENSO teleconnections from a regional phenomenon affecting mainly North America into NAM-like events with hemispheric extent.

An increasing body of research has shown that seasonal variations in the NAM depend on the phasing (linear interference) of extratropical planetary waves (Nishii et al. 2011; Garfinkel and Hartmann 2008; Smith et al. 2010; FK13, FK11; Kim et al. 2014). Briefly, all of these studies conclude that when anomalous waves associated with surface forcing—primarily in the tropics—amplify (damp) the climatological waves, the polar vortex is weakened (strengthened), causing a negative (positive) NAM response. Linear interference is found to explain a large fraction of the variance in NAM responses arising from tropical forcing experiments with multiple different model configurations (FK13). It has been known for some time that ENSO–NAM teleconnections are sensitive to many aspects of a model's basic state, including the location and intensity of the subtropical and eddy-driven jets (Ting et al. 1996), and the emerging consensus is that detailed knowledge of the phase and amplitude of a model's extratropical stationary waves can provide important additional information in this regard (FK13).

It is well appreciated that tropical precipitation drives atmospheric teleconnections originating in the tropics (Annamalai et al. 2005) and therefore also the NAM response. In the tropics, SST determines precipitation anomalies mainly over the central and eastern Pacific; elsewhere, such as over much of the TIO, precipitation is more independent of SST. However, the west and southwest TIO have also been identified as source regions for teleconnections with the northern extratropics (Annamalai et al. 2007). Recent analysis of teleconnections originating from the TIO sector shows quite different response patterns in the extratropics depending on whether the teleconnections are defined with respect to SST or precipitation anomalies. This is because the precipitation anomalies over the TIO are largely independent of ENSO, whereas SSTs over TIO are not (Molteni et al. 2015). In addition, recent discussion of the connection between the TIO and global climate has focused on the Indian Ocean dipole (IOD). While a significant portion of IOD variability is explained by ENSO, the IOD also projects onto other patterns of internal variability operating purely within the TIO (Saji et al. 1999). Several different types of IOD events have recently been identified, including a type that is statistically independent of ENSO (Guo et al. 2015). Collectively, the clear implication is that atmospheric variability generated by SST/precipitation anomalies internal to the TIO can, when not competing with ENSO conditions, induce teleconnection anomalies with the northern extratropics (Annamalai et al. 2007).

It is important to note that the vast majority of the modeling studies cited above use prescribed SST anomalies to simulate teleconnections, leaving some doubt as to whether observed SST anomalies in the TIO (generated in response to IOD events, climate change, and SST anomalies in the TEP associated with ENSO) can actually drive atmospheric teleconnections in nature (Deser and Phillips 2006; Copesey et al. 2006). Here, we study the problem of TIO influence on ENSO teleconnections using a model that includes a fully interactive ocean component. After first presenting details

of our methods and numerical experiments (section 2), we examine ENSO–NAM teleconnections in a long freely running preindustrial control experiment (section 3) and then investigate the dynamical details of the NAM response using a nudging technique to impose realistic ocean temperatures separately in the TIO and TEP (section 4). Our contribution is to provide the strongest evidence yet that SST anomalies and associated diabatic heating over the TIO play an active role in modulating ENSO–NAM teleconnections through changes to the phase and amplitude of extratropical planetary waves.

2. Data and methods

a. Model and experimental design

The model used in this study is CNRM-CM5, the fifth generation coupled ocean–atmosphere GCM developed by Météo-France and the Centre Européen de Recherche et de Formation Avancée en Calcul Scientifique (CERFACS). Full details of the model formulation are provided in Voltaire et al. (2013), but, briefly here, the atmospheric component is ARPEGE-Climat-5.2, which is a spectral model run at a horizontal resolution of T127 (approximately $1.4^\circ \times 1.4^\circ$ latitude–longitude) with 31 vertical layers and a lid at 10 hPa (approximately 30 km). The ocean component is NEMO version 3.2 (Madec 2008), run at a horizontal resolution of approximately $1^\circ \times 1^\circ$ with 42 vertical layers. Tropical–extratropical teleconnections are investigated with CNRM-CM5 using two complimentary approaches, described below.

1) PREINDUSTRIAL CONTROL COMPOSITE ANALYSIS

The first approach uses the output from a 1000-yr preindustrial control integration (piControl), where all external climate forcings are fixed at 1850 levels. To create piControl, the model was initially spun up for 200 yr with fixed 1850 forcing, starting from a present-day ocean climatology. After verifying that this spinup had resulted in equilibration to the 1850 climate, the integration was continued for a further 1000 yr, and those data are analyzed in section 3. The model does not include a flux correction term to balance energy fluxes, which results in a minor energy imbalance at the ocean–atmosphere surface of 0.38 W m^{-2} , leading to a modest drift in annual mean three-dimensional ocean temperatures in piControl ($0.04 \text{ K century}^{-1}$) (Ruprich-Robert and Cassou 2014). To mitigate sampling biases due to this drift, we linearly detrended all data from piControl prior to performing our analyses. However, we have verified that the trends are sufficiently small that our

results remain virtually identical when the trend is included (not shown).

We are interested in isolating the teleconnection and NAM response to convective forcing from the tropical east Pacific and Indian Ocean basins. To this end, we create composites of winters from piControl based on the magnitude of spatially averaged December–February (DJF) mean tropical precipitation anomalies P' in each basin. We define P' as the deviation of each month's mean precipitation from the climatological mean precipitation for that month, calculated over the entire 1000-yr integration. The averaging regions are based on Molteni et al. (2015): for TEP we include the area bounded by 10°S – 10°N , 160°E – 150°W , while for TIO the area is 10°S – 10°N , 40° – 80°E , which roughly corresponds to the western half of the basin where P' has been linked to teleconnections (Annamalai et al. 2007).

A winter is classified as “active” in a particular basin when $|P'| > \sigma_a$, where $|\dots|$ denotes the absolute value (magnitude), and σ_a is a precipitation threshold determined separately for TEP and TIO by their 20th/80th percentile values, yielding a combined subset of 400 active winters for each basin. The lower percentile corresponds to extreme negative (dry) winters and the higher percentile to extreme positive (wet) winters. In addition, we define a subset of 200 “neutral” winters in each basin, where precipitation anomalies lie between the 40th and 60th percentiles. By selecting conditionally from these subsets for TEP and TIO, we construct three composite groups containing the following: (i) 168 winters (84 wet, 84 dry) with active, same-signed P' in both basins simultaneously ($P_a I_a$ cases); (ii) 66 winters (30 wet, 36 dry) with active P' in TEP and neutral conditions in TIO ($P_a I_n$ cases); and (iii) 57 winters (27 wet, 30 dry) with neutral conditions in TEP and active P' in TIO ($P_n I_a$ cases). We tested an alternative method using DJF SST anomalies, rather than P' , over TEP and TIO. However, we found that SSTs in the two basins are highly correlated ($r = 0.76$) because SSTs in TIO tend to have the same sign as ENSO-related anomalies in TEP (Trenberth et al. 2002). This alternative was therefore rejected because it led to a paucity of $P_n I_a$ cases, making it challenging to isolate the influence of TIO-induced teleconnections. Using P' is advantageous because the correlation between precipitation anomalies in the two basins is weaker ($r = 0.48$) than for SST. Molteni et al. (2015) found a similar correlation when analyzing a different coupled GCM but noted that in observations this relationship is actually much weaker ($r = 0.19$). The implication is that models overestimate the influence of ENSO on TIO precipitation, and therefore our model-derived estimates of independent NAM teleconnections generated from the TIO may be somewhat conservative.

The climate and NAM responses for each composite group are then defined as the mean difference between the anomalies in the wet and the dry winters, averaged over all winters in a group. Our methodology therefore implicitly assumes linearity between the wet and dry phases of each group; the figures and discussion are presented for the “wet” (high threshold) cases under the assumption that the signals are opposite signed for the “dry” (low threshold) cases. Statistical significance of the difference is assessed using a Student’s t test. We have verified that our conclusions are broadly insensitive to varying the composite size over the range $10 < n < 100$ (achieved by adjusting the percentile thresholds). Finally, we also tested the effect of filtering out subdecadal variability in the precipitation time series used to formulate the composites. Despite considerable decadal variability being present in piControl, our composite thresholds are chosen such that extreme winters tend not to cluster together and, as a result, our conclusions are found to be insensitive to this filtering.

2) OCEAN NUDGING EXPERIMENTS

The second approach is to isolate the impact of TIO and TEP SST anomalies on NAM teleconnections by conducting so-called “pacemaker” experiments (Cash et al. 2008), where the ocean temperatures in each region are nudged toward an oceanic reanalysis dataset. Two sets of 24-month integrations were performed, one from 1 January 1997 to 31 December 1998 simulating the evolution of the 1997/98 El Niño (warm event) and another from 1 January 1998 to 31 December 1999 simulating the evolution of the 1998/99 La Niña (cold event). For each of the warm/cold events, two nudging experiments were performed with nudging applied over: (i) the TEP region (NUD_{PAC}), and (ii) the TIO region (NUD_{IND}). In all regions not being nudged, the ocean model was freely coupled with the atmosphere. While the choice of years for the nudging is relatively obvious for NUD_{PAC}, we nudge for the same years in NUD_{IND} because a large interannual shift of the IOD occurred during the 1997–99 ENSO cycle (Saji et al. 1999).

This setup yields a set of four unique experiments: 1) NUD_{PAC} warm, 2) NUD_{PAC} cold, 3) NUD_{IND} warm, and 4) NUD_{IND} cold. The response for the two nudging regions is calculated as the difference between the wet and dry experiments (i.e., for NUD_{PAC}, it is computed as experiment 1 minus experiment 2). The nudging integrations branched from 1 January restart files extracted from 20 consecutive years in piControl starting at year 498, forming a set of $n = 20$ ensemble members for each experiment. The 20-yr period 498–517 was selected from piControl because it displayed generally weak ENSO activity and near-neutral anomalies in tropical ocean

heat content. In this way, we minimize the interference between the nudging and the internally generated ENSO activity in piControl. All other boundary conditions are held fixed at 1850 levels after branching (i.e., they remain identical to piControl).

Nudging is applied using the NEMO model’s built-in restore functionality, following Sanchez-Gomez et al. (2015). The ocean model’s temperature and salinity below the mixed layer are nudged toward the NEMO variational data assimilation system (NEMOVAR) three-dimensional ocean reanalysis (Morgensen et al. 2009) using a Newtonian restoring time scale of 10 days. At the surface, a flux derivative term is used for temperature ($-40 \text{ W m}^{-2} \text{ K}^{-1}$) and salinity (167 mm day^{-1}). For NUD_{PAC} the nudging region is 10°S – 10°N , 180° – 60°W , and for NUD_{IND} the nudging region is 10°S – 10°N , 40° – 120°E . The nudging region in NUD_{IND} corresponds to the same longitudinal extent as the domain used in previous experiments investigating the role of the Indian Ocean on teleconnections using prescribed SSTs (FK11, FK13). To avoid singularities at the boundary of the nudging region, we apply a buffer zone of 20° on all sides; in this zone, the restoring term decreases to zero as a Gaussian function of latitude or longitude (depending on whether it is a zonal or meridional boundary). The temperature and salinity in the buffer zone are determined by a linear combination of the ocean model calculation and the reanalysis.

The intent of these experiments is to dissect, in a coupled model framework, the teleconnection and NAM response to localized precipitation anomalies over the two basins. We acknowledge that the experimental setup is idealized, and therefore the results may not be fully representative of the real atmosphere. However, the inclusion of realistic time-varying forcing, and atmosphere–ocean coupling within and outside of the tropics provides a significant increase in realism compared to previous work using prescribed time-invariant global SST anomalies (e.g., FK11, FK13). An alternative protocol could have been to nudge the atmospheric fields over the domains of interest in order to generate precipitation and diabatic heating anomalies independently from SST changes. However, the regional nudging functionality in ARPEGE was not available at that time of our study.

b. Scaling of results

In the piControl composites, the $P_a I_n$ and $P_a I_a$ groups (i.e., those with active $|P'$ in the tropical Pacific) are associated with ENSO events, and the mean anomalies in these two groups are significantly larger than in the $P_n I_a$ cases. To properly compare the teleconnections and NAM responses across these three sets of cases, we

TABLE 2. Table comparing ENSO variability in CNRM-CM5 (1000-yr piControl simulation) and observations (HadISST 1901–2000).

Diagnostic (unit)	Observations	CNRM-CM5
Standard deviation (K)	0.91	0.93 (± 0.04)
Maximum (K)	2.38	2.05 (± 0.12)
Minimum (K)	–1.88	–1.90 (± 0.15)
$p(90\text{th})$ (K)	1.20	1.34 (± 0.10)
$p(10\text{th})$ (K)	–1.23	–1.20 (± 0.08)
frequency > 1.0 K (fraction)	0.14	0.17 (± 0.02)
frequency < -1.0 K (fraction)	0.13	0.15 (± 0.02)

employ a simple scaling of $1/\tau$ on each variable shown, where τ is computed as $|P'|$ averaged over the entire tropical belt (20°S – 20°N) for the wet-minus-dry phase of each group. The values of τ are 2.60, 1.49, and 0.67 mm day^{-1} for P_{aI_a} , P_{aI_n} , and P_{nI_a} , respectively. We apply the same scaling to the output from the nudging experiments, where the imposed SST forcing averaged over the tropical belt in NUD_{PAC} is more than twice as strong as in NUD_{IND} . The τ values for the nudging experiments are 1.81 mm day^{-1} for NUD_{PAC} and 1.04 mm day^{-1} for NUD_{IND} . The rescaling of all variables (except for the heat flux decomposition shown in Fig. 9) means that our results are expressed as anomalies per unit tropical $|P'|$. However, this scaling turns out not to be particularly important for our conclusions, because we will demonstrate that the sign and spatial patterns of the response can be of opposite sign depending on whether the TIO basin is active, or not.

c. ENSO variability in piControl

Before evaluating tropical–extratropical teleconnections in piControl, we first assess the representation of ENSO in CNRM-CM5, to establish how well tropical variability is simulated in this model. Observed variability in ENSO SSTs, as represented by HadISST data 1901–2000 (Rayner et al. 2003), is well reproduced by the model: the observed amplitude and frequency of Niño-3.4 events exceeding ± 1 K generally lie within the simulated range of estimates from 10 consecutive 100-yr segments from the 1000-yr integration of piControl, designed to mimic the observational period (Table 2). The main exception is the strength of the maximum warm event on record, which in observations is the 1997/98 event, and whose amplitude is found to be around 15% larger than the model’s strongest event. This bias in SST variability could have implications for our analyses, since, in the warm phase nudging experiments [section 2a(2)], we force the model with ocean temperatures derived from the 1997/98 event, and this forcing is likely to lie outside of the model’s range of internal variability. This effect is further demonstrated by noting that

τ (derived from precipitation anomalies; section 2b) is $\sim 20\%$ stronger in NUD_{PAC} than in P_{aI_n} and $\sim 55\%$ stronger in NUD_{IND} than in P_{nI_a} . We will demonstrate in section 4c that the strength of the forcing/response in the nudging experiments may be linked to increased nonlinearity in the teleconnection and NAM responses.

d. Diagnosing linear interference

Two methods are employed to diagnose the linear interference of Rossby waves. The first is a full decomposition of the eddy meridional heat flux, as documented in Smith et al. (2010) and FK13. Briefly here, this method takes 6-hourly mean output for the three-dimensional eddy meridional wind v^* and temperature T^* and computes their covariance v^*T^* based on a Reynolds decomposition.¹ Seasonal variations in the polar vortex can be related to v^*T^* through the upward component of the Eliassen–Palm flux entering the stratosphere (Andrews et al. 1987). The total response of v^*T^* (TOTAL) in an ensemble of realizations is given by

$$\Delta\{\langle v^*T^* \rangle\} = \text{TOTAL},$$

where the braces denote the time and zonal mean, the angle brackets denote the ensemble mean over all realizations, Δ denotes the response (perturbed minus control, or warm phase minus cold phase). TOTAL can be decomposed into an ensemble mean component (EM) and a component representing the fluctuations of v^*T^* in each realization around the ensemble mean (FL):

$$\text{TOTAL} = \text{EM} + \text{FL},$$

$$\text{EM} = \Delta\{\langle v^* \rangle \langle T^* \rangle\}, \quad \text{and}$$

$$\text{FL} = \Delta\{\langle v'^* T'^* \rangle\},$$

where the prime denotes the deviation from the ensemble mean. The EM term can be decomposed further into

$$\text{EM} = \text{EM}_{\text{LIN}} + \text{EM}_{\text{NL}},$$

where, if the subscript c denotes the 1000-yr climatological stationary wave from piControl,

$$\text{EM}_{\text{LIN}} = \{v_c^* \Delta\langle T^* \rangle\} + \{\Delta\langle v^* \rangle T_c^*\} \quad \text{and}$$

$$\text{EM}_{\text{NL}} = \{\Delta\langle v^* \rangle \Delta\langle T^* \rangle\}.$$

¹ Instantaneous data are preferred over time mean data for computing eddy covariances, because time averaging can damp the fluxes; however, only 6-hourly time mean data were available as output from our nudging experiments. Based on prior analysis comparing covariances calculated using daily mean and daily instantaneous values, the use of 6-hourly means instead of instantaneous output likely underestimates the covariance by $<10\%$.

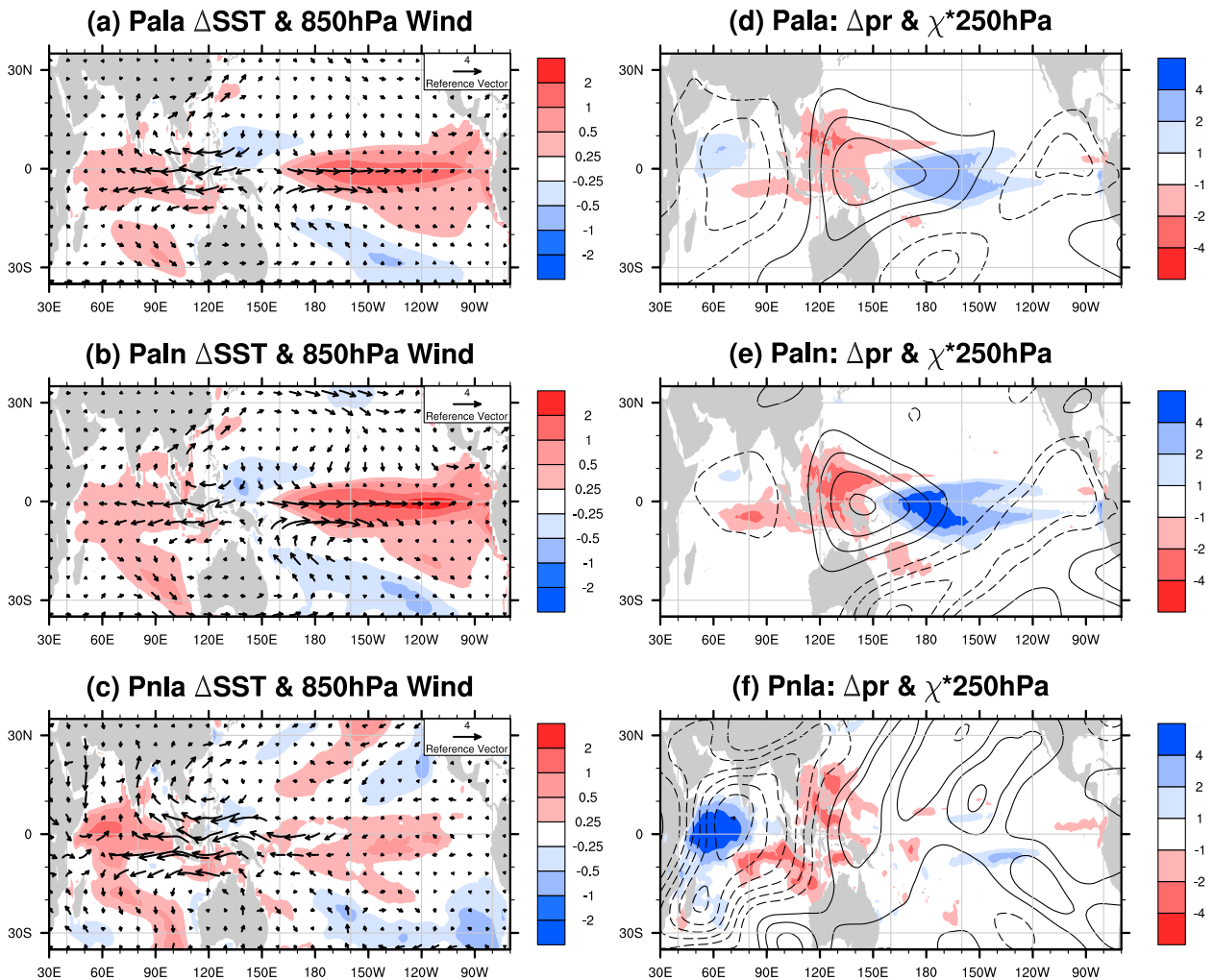


FIG. 1. Tropical–subtropical December–February mean anomalies for different variables in (top) P_{aI_a} , (middle) P_{aI_n} , and (bottom) P_{nI_a} . (left) The ΔSST (shading) and 850-hPa wind vectors (reference vector is 4 m s^{-1}). (right) The precipitation anomalies (Δpr ; shading; note, blues are positive) and the eddy velocity potential at 250 hPa ($\Delta\chi^*250\text{hPa}$; contours; interval is $1 \times 10^6 \text{ m}^2 \text{ s}^{-2}$; negative values are dashed).

EM_{LIN} depends on the linear interference, or the phase difference, between the anomalous, or response, wave and the climatological stationary wave; and EM_{NL} depends on the amplitude of the wave response and is always positive because it is quadratic in wave amplitude.

Submonthly frequency output were not available from the full 1000-yr piControl integration, so we also diagnose linear interference using the pressure-weighted correlation r_{zp} in each month between the anomalous eddy geopotential height at 60°N ($Z^*60^\circ\text{N}$) and its climatological mean ($Z^*60^\circ\text{N}_{\text{clim}}$). The weights are based on the relative thickness of each of the vertical layers from 850 to 10 hPa. The correlation is computed separately for the zonal wavenumber 1 and 2 components of $Z^*60^\circ\text{N}$, which are filtered using a Fourier transform.

3. Tropical–extratropical teleconnections in the piControl composites

a. Tropical convection and Rossby wave generation

We first compare the DJF mean tropical anomalies in the three sets of piControl composites. The patterns in the P_{aI_a} and P_{aI_n} cases (collectively, the Pa-type cases) are highly similar, since both cases are associated with ENSO events. Warm SSTs in the eastern Pacific are maintained by westerly wind anomalies along the equator, causing lower-tropospheric convergence, ascent, and increased precipitation centered on the date line (Figs. 1a,b,d,e). Cooler SSTs over the western Pacific and Maritime Continent are associated with an area of anomalous subsidence and lower-level divergence. The most important difference between these cases is

that, in P_{aI_a} (i.e., the case with larger magnitude Indian Ocean precipitation anomalies by design), anomalous easterly winds from the Maritime Continent are stronger and penetrate deeper into the TIO, leading to stronger ascent and precipitation there. Compared to the pattern in P_{aI_n} , the P_{aI_a} anomalies in $Z^*250\text{hPa}$ thus project more strongly onto a zonal wavenumber 2 pattern. In P_{aI_n} , both OLR and $Z^*250\text{hPa}$ are reinforced over the western and central Pacific. The anomalous subsidence in the western Pacific is symmetrically compensated on both flanks in P_{aI_a} but is confined to the TEP sector in P_{aI_n} (Figs. 1d,e). Our interpretation of the differences between the Pa-type cases is that P_{aI_n} represents the canonical response to ENSO, which is dominated by reduced precipitation over much of the TIO, whereas P_{aI_a} captures the response to ENSO plus a component of internal variability generated over the TIO.

The P_{nI_a} case is very different to the Pa-type cases, with stronger SST and circulation anomalies located over the TIO and relatively weak anomalies over the tropical Pacific (Figs. 1c,f). We note the presence of weak ($\sim 0.25\text{ K}$) same-signed SST anomalies in the tropical Pacific (Fig. 1c), indicating that the P_{nI_a} case is not simply capturing the inverse of Pa-type cases (i.e., La Niña). The tropical atmosphere shows strong convection and upper-tropospheric divergence occurring across the entire TIO, even though the precipitation anomalies form an east–west dipole that projects onto the Indian Ocean dipole mode of variability (Saji et al. 1999). This is consistent with the strong easterly anomalies in 850-hPa wind across the entire Maritime Continent, leading to strong convergence around 60°E , where anomalous SST anomalies are the greatest.

In the tropics and subtropics, the Pa-type cases also have similar spatial structure in 250-hPa wave geopotential height ($Z^*250\text{hPa}$), with each case showing a wave train radiating poleward out of the central Pacific that projects onto the positive phase of the Pacific–North American (PNA) pattern (Figs. 2a,b). However, the P_{aI_n} case (i.e., with neutral Indian Ocean precipitation) shows a much deeper negative anomaly in the Aleutian low region that is shifted around 15° west (Fig. 2c). This is consistent with the stronger, zonally confined, diabatic heating anomalies in P_{aI_n} acting as a Rossby wave source for the North Pacific (Fig. 1e). Just as with the tropical convective response, the wave pattern in P_{nI_a} (the neutral Pacific case) is radically different to the Pa-type cases, radiating poleward and eastward out of the northwest TIO (Fig. 2c). We note the lack of statistically significant anomalies in P_{nI_a} , which is related to the relatively small amplitude of the extratropical wave response in this case (recall that all

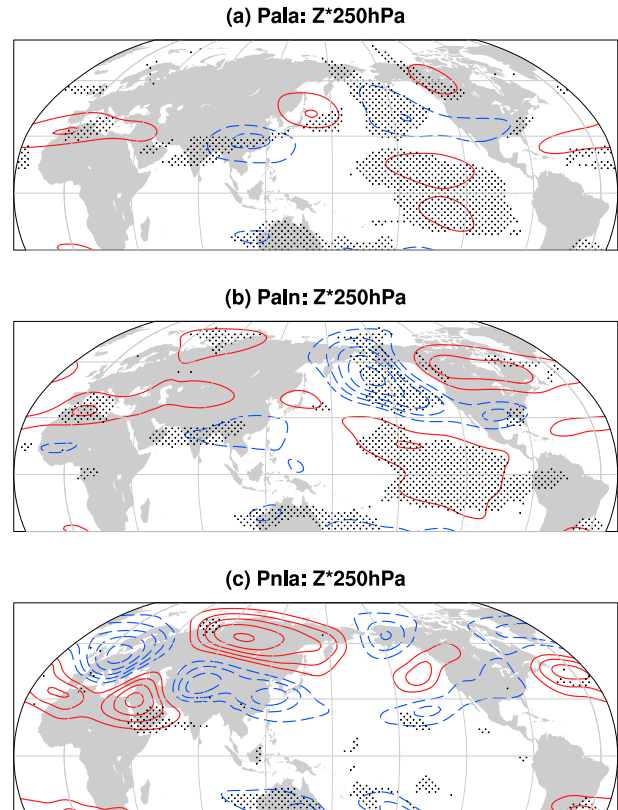


FIG. 2. December–February mean 250-hPa eddy geopotential height ($Z^*250\text{hPa}$) anomalies in (top) P_{aI_a} , (middle) P_{aI_n} , and (bottom) P_{nI_a} . Positive (negative) values are shown by red solid (blue dashed) contours; contour interval is 10 m. Stippling indicates where the response is significantly different from zero ($p < 0.05$).

panels are scaled per unit tropical precipitation anomaly; see section 2b). However, we show in section 4 that this type of wave pattern is a robust feature of the ocean nudging experiments, so we are confident that it is not simply the result of sampling variability.

b. Linear interference and the NAM response

We next examine the relationship between planetary wave interference—evaluated through the entire depth of the troposphere and lower stratosphere—and the NAM, using zonal mean zonal wind ($[u]$) anomalies at 60°N as a proxy for the NAM. The anomalous wave in P_{aI_a} is confined primarily to the stratosphere and is in quadrature with Z^*_{clim} for both wave 1 ($r_{z_p} = -0.06$) and wave 2 ($r_{z_p} = -0.12$) (Figs. 3a,b). The polar vortex response in P_{aI_a} is very weak and not statistically significant (Fig. 3c). In P_{aI_n} the anomalous wave 1 projects strongly onto Z^*_{clim} ($r_{z_p} = 0.92$) and projects weakly onto wave 2 ($r_{z_p} = -0.31$) (Figs. 3d,e). Since the magnitude of the anomalous wave is small compared to Z^*_{clim} , this pattern of positive wave-1 linear interference would normally indicate increased wave activity flux (WAF)

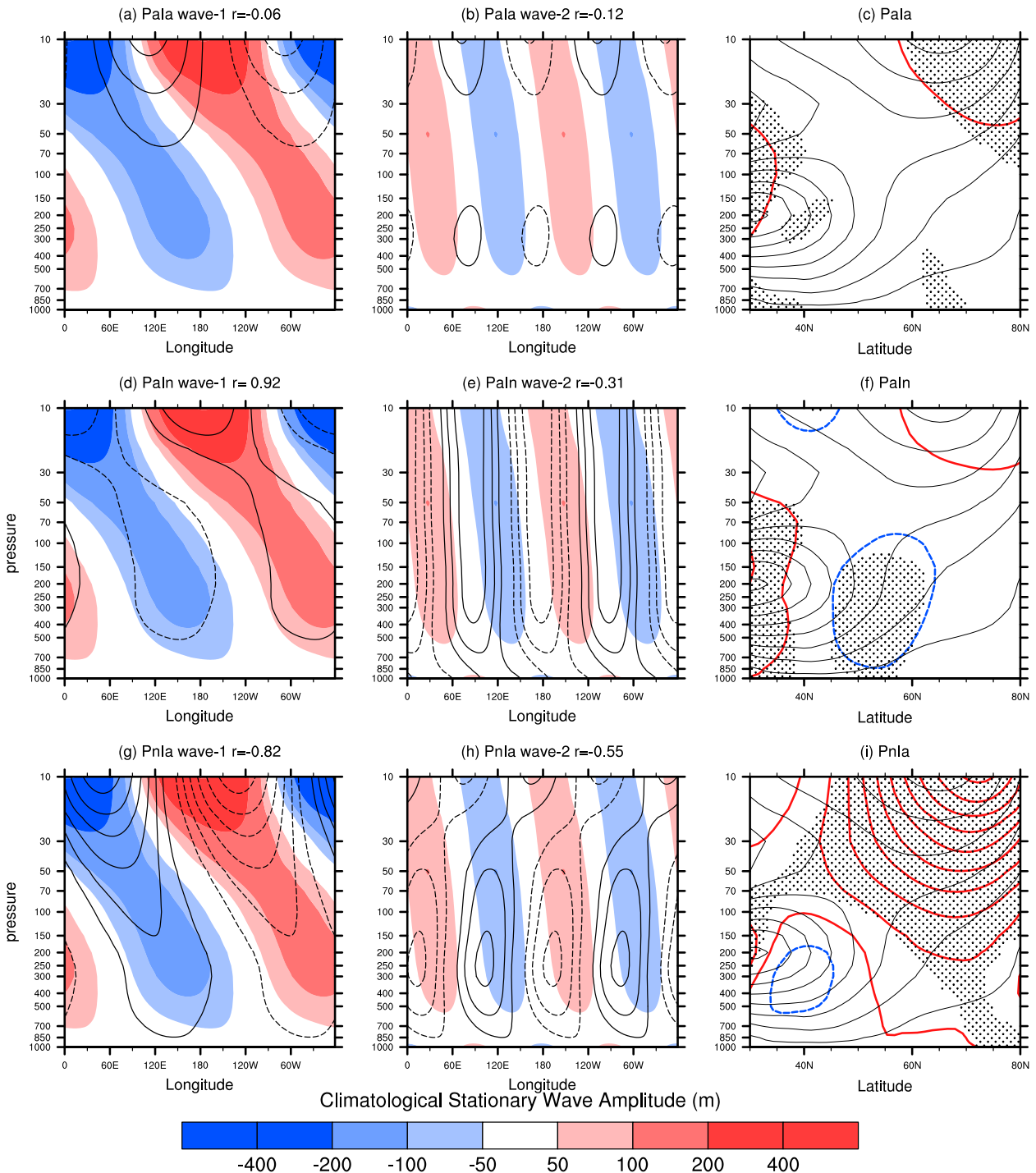


FIG. 3. (left),(center) December–February mean wave geopotential height cross sections at 60°N ($Z^*60^{\circ}\text{N}$), and (right) zonal mean zonal wind anomalies $30^{\circ}\text{--}80^{\circ}\text{N}$ ($[\Delta u]$) in (top) P_aI_a , (middle) P_aI_n , and (bottom) P_nI_a . The left panels show the wave-1, and the center panels show the wave-2 components of $Z^*60^{\circ}\text{N}$. Shading shows the climatological mean $Z^*60^{\circ}\text{N}$ with red (blue) indicating positive (negative) values. Contours show the $Z^*60^{\circ}\text{N}$ composite anomalies for wet-minus-dry phases [see section 2a(1)]; contour interval is 20 m for wave 1 and 10 m for wave 2, and negative values are dashed. The right panels show the climatological zonal mean zonal wind (black contours; interval is 5 m s^{-1}) and $[\Delta u]$ (blue and red contours; interval is 0.5 m s^{-1} , with blue dashed contours showing negative values). Stippling indicates areas where $[\Delta u]$ is significantly different from zero ($p < 0.05$).

entering the polar stratosphere. Yet it is intriguing that, just as in P_aI_a , there is no significant polar vortex anomaly in P_aI_n (Fig. 3f). However, we do note a weak but significant negative $[u]$ anomaly in the midlatitude troposphere, consistent with an equatorward-shifted midlatitude jet and a negative NAM in the lower atmosphere (Thompson and Wallace 2000).

As expected from the $Z^*250\text{hPa}$ pattern, in P_nI_a we see broadly the opposite signal to the P_a -type cases, with a strong negative projection of the anomalous wave onto Z^*_{clim} in both waves 1 and 2, indicating destructive linear interference (Figs. 3g,h; $r_{zp} = -0.82$ and $r_{zp} = -0.55$, respectively). This pattern of linear interference should damp Z^*_{clim} , reducing the total WAF entering the polar stratosphere, strengthening the polar vortex. This appears to be exactly what we find: the clearest difference in P_nI_a compared to the P_a -type cases is the very strong positive $[u]$ anomalies, peaking in the polar stratosphere, that indicate a significant positive NAM signal (Fig. 3i). The positive NAM pattern extends down into the troposphere and couples with the surface around 50°N , suggesting a poleward shift of the tropospheric jets and an intensified polar vortex.

In summary, active precipitation anomalies over the TIO are associated with robust and significant changes in the patterns of wintertime Rossby wave interference and associated $[u]$ anomalies. Convective forcing from the TIO appears to shift the wave-1 component of $Z^*60^\circ\text{N}$ toward destructive interference, counteracting the constructive interference arising in response to the canonical ENSO forcing [P_aI_a ; see Fig. 3d; Ineson and Scaife (2009); FK11]. In the wave-2 component of $Z^*60^\circ\text{N}$, the picture is less clear: in the P_a -type cases, the presence of an active TIO causes increased constructive interference, yet, confusingly, the wave-2 response to TIO forcing independent of ENSO (P_nI_a) shows strong destructive interference (see Fig. 3c and FK11). The difference between this analysis and that of FK11 is that here the tropical convective forcing evolves in time, whereas FK11 used perpetual SST anomalies integrated throughout the DJF season. In the next section, we examine intraseasonal variation in the piControl responses to gain a better understanding of how these more realistic cases evolve.

c. Intraseasonal variation in the NAM response

The time evolution of the NAM anomalies from each case in the troposphere and stratosphere is depicted by $[u]$ at 60°N in Fig. 4. The P_aI_a case shows a weak positive NAM signal in the stratosphere during December–January, but no response in any other months or in the troposphere (Fig. 4a). For the P_aI_n case, the NAM anomalies evolve into a pattern resembling a negative

stratosphere–troposphere NAM in February–March (Fig. 4b), although it is quite weak and not statistically significant outside of the troposphere. These results are broadly similar to those of Bell et al. (2009), who highlighted that the response to ENSO in a model simulation with a well-resolved stratosphere transitioned from a weak positive NAM/North Atlantic Oscillation (NAO) in mean sea level pressure during November–December to a strong negative response in January–February. In our results, cancellation between a positive NAM in November–December (although not significant and limited to the stratosphere) and a negative NAM in February–March that is more barotropic but still not significant above 100 hPa, explains why the DJF mean $[u]$ in P_aI_n shows such a weak signal in the polar stratosphere (Fig. 3f). By contrast, the NAM response in P_nI_a is strong and positive throughout the winter, with the signal peaking in the stratosphere during January–February and progressing downward and coupling strongly with the surface during February–March.

The relationship between linear interference and the monthly NAM response is explored using the r_{zp} metric. For P_aI_a , the interference patterns are generally in quadrature, except during December, when strong destructive interference from waves 1 and 2 implies reduced WAF entering the polar stratosphere (Fig. 4a). This wave-driving event coincides with the brief positive NAM episode in the stratosphere, which quickly dissipates as the wave interference during January–March becomes transient and unstructured. The P_aI_n case tends more toward constructive interference, particularly in wave 1 from January–March (Fig. 4b). This wave pattern implies increased WAF into the stratosphere, which is consistent with planetary wave driving of the weak negative NAM signal beginning in the stratosphere in February and seen in the troposphere all winter. By contrast, the interference patterns in the P_nI_a case are consistently destructive in waves 1 and 2 (i.e., negative r_{zp}) for most of the winter (Fig. 4c). Again, the linear interference patterns appear to lead the stratospheric NAM response by around one month, which is consistent with perturbation of the polar vortex by Rossby waves propagating up from the troposphere (Charney and Drazin 1961).

Using the results from our three groups of cases, we speculate here on the apparent roles for Indian Ocean versus Pacific precipitation anomalies in driving wave interference and NAM anomalies. Assuming that our P_aI_n and P_nI_a cases represent the signal associated with active precipitation in a single basin, then, if the precipitation anomalies in the two basins act additively, P_aI_a should represent some linear combination of P_aI_n and P_nI_a . Broadly speaking, our findings are consistent with

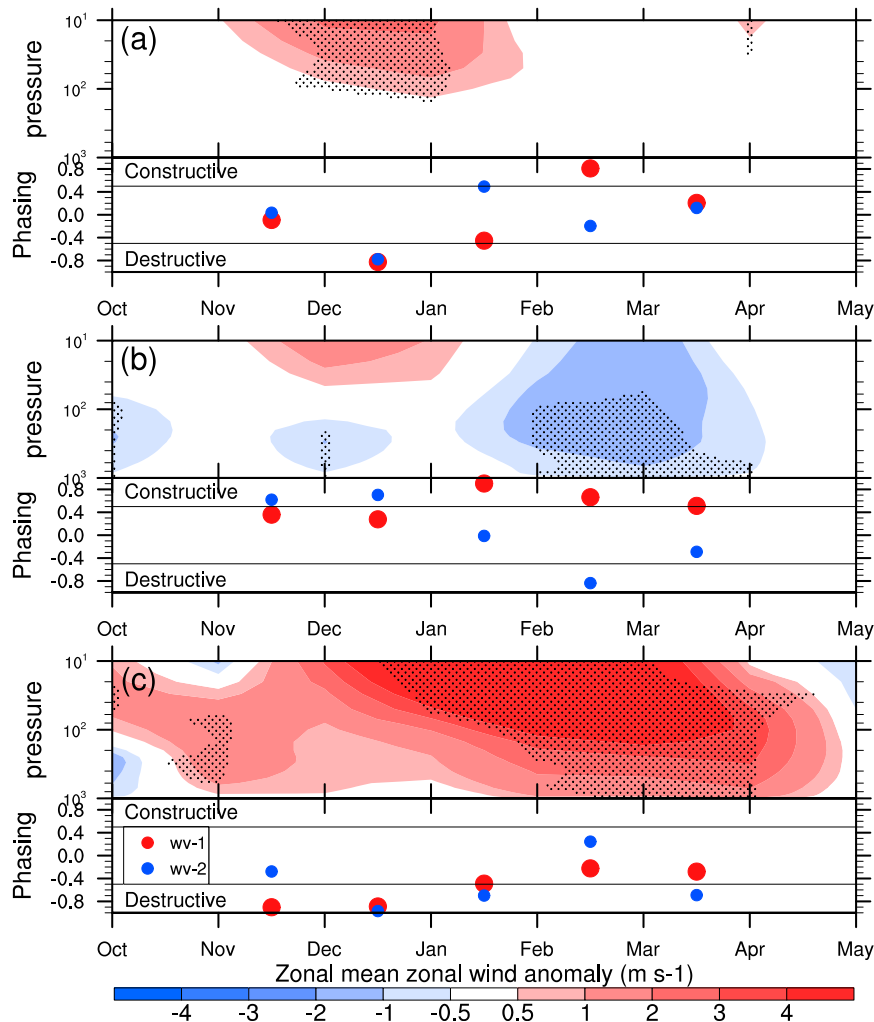


FIG. 4. Upper half of each panel shows the time–height cross section of the monthly zonal mean zonal wind anomalies at 60°N (color shading; m s^{-1}), with stippling indicating areas where the wind anomalies are significantly different from zero ($p < 0.05$) for (a) P_aI_a , (b) P_aI_n , and (c) P_nI_a . Lower half of each panel shows the pressure-weighted correlation r_{zp} (see section 2d) for wave 1 (red) and wave 2 (blue). A threshold of $r_{zp} = 0.5$ ($r_{zp} = -0.5$) is used to denote months as having constructive (destructive) linear interference.

these assumptions. When the Pacific is active alone (P_aI_n), the linear interference is constructive later in the season (Fig. 4b), while, when the Indian Ocean is active alone (P_nI_a), the linear interference is destructive earlier in the season (Fig. 4c). When the two basins are active together (P_aI_a), the early season response resembles that from P_nI_a , while the late season response involves considerable cancellation and no discernible NAM response (Fig. 4a). The clear implication is that the presence of precipitation anomalies in the TIO in P_aI_a weakens the constructive interference initiated from the Pacific, particularly in wave 1.

To understand the origin of the intraseasonal variation in the wave interference and NAM signals in

each case, it is informative to examine the time evolution of the tropical SST and precipitation anomalies. As demonstrated in Fig. 1, the Pa-type cases clearly capture significant ENSO events, and this is reflected in their time-evolving SST anomalies, which are highly similar (Figs. 5a,b). However, the P_aI_a case involves a more zonally symmetric precipitation signal (i.e., the peaks in precipitation over TIO and TEP are more similar in magnitude) compared to the P_aI_n cases (i.e., the peaks in precipitation over the Pacific and small anomalies over the TIO (Fig. 5e)). On the other hand, the P_nI_a cases do not describe ENSO events during DJF (Fig. 1c); however, these cases transition into La Niña events during

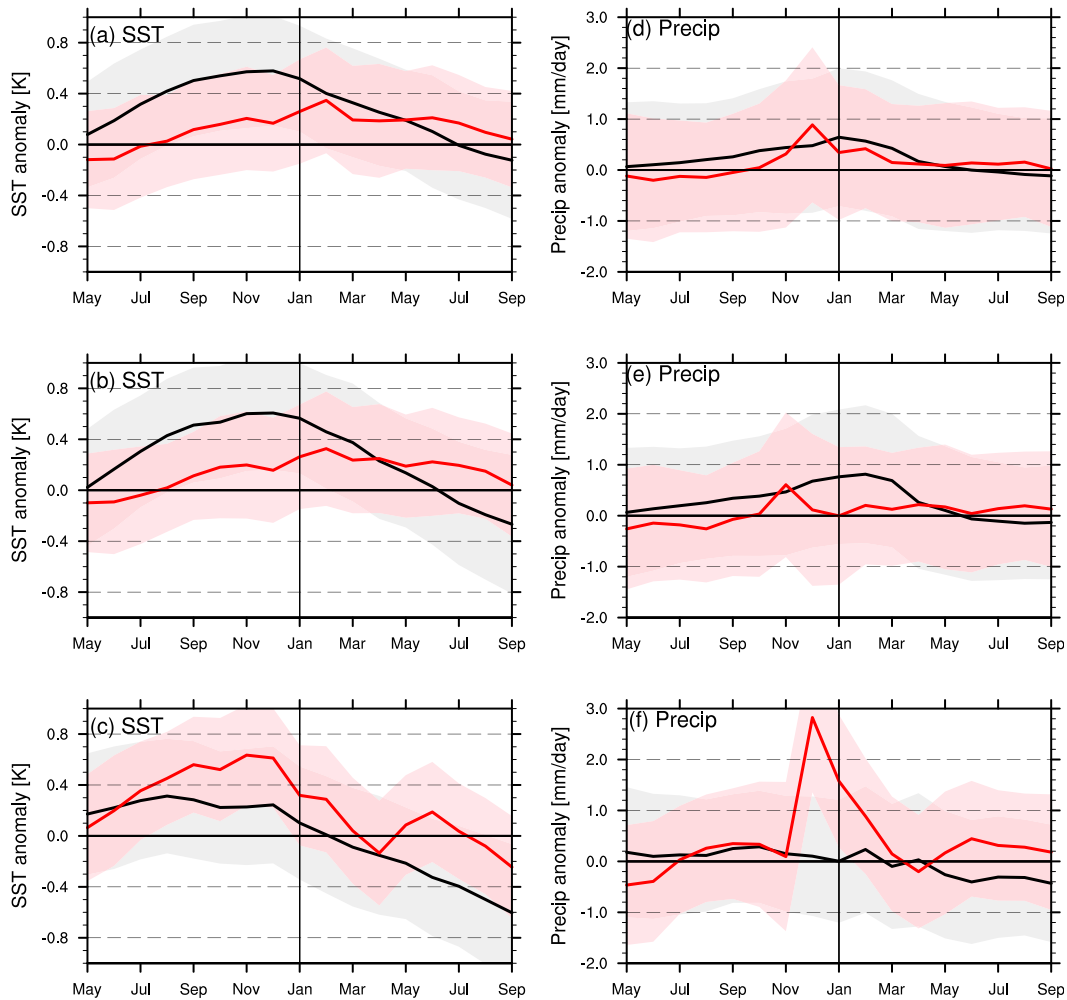


FIG. 5. May–September monthly mean (left) sea surface temperature (K) and (right) precipitation (mm day^{-1}) averaged over the tropical (20°S – 20°N) Indian Ocean (red lines) and eastern Pacific Ocean (black lines) for the (top) P_nI_a , (middle) P_nI_n , and (bottom) P_nI_a . The shaded region around each solid line indicates the intracomposite variability represented by one standard deviation around the composite mean. The panels are centered on the January in the middle of the compositing period, denoted by a vertical black bar in the center of each panel.

the following summer/fall (Fig. 5c). This is consistent with the P_nI_a cases representing positive IOD events, which are thought to be triggers for La Niña events (Izumo et al. 2010). It is intriguing that all three groups of cases produce wintertime peaks in precipitation over the western TIO (red lines in Figs. 5d–f): in the active TIO cases, the peak occurs in December, while in P_nI_n , the peak is weaker and occurs one month earlier so that, by DJF (the period for which the composites are constructed), there is neutral precipitation over the TIO. The fact that this peak can occur independently of ENSO (Fig. 5f) further reinforces the idea that the TIO is able to generate internal variability that has the potential to drive teleconnections.

4. Tropical–extratropical teleconnections in the nudging experiments

a. Tropical convection and Rossby wave generation

From the results presented above, the suggestion is that the location of tropical precipitation anomalies exerts a control over the pattern of wave interference, and thus the NAM response, to forcing from the tropical Indian and Pacific Oceans. In this section, we describe the results of our nudging experiments, in which we explicitly initiate precipitation anomalies over the TEP (NUD_{PAC} experiment) and TIO (NUD_{IND} experiment) to study their separate effects on the NAM. We present ensemble mean results indicating that internal variability generated outside of the nudging region is suppressed

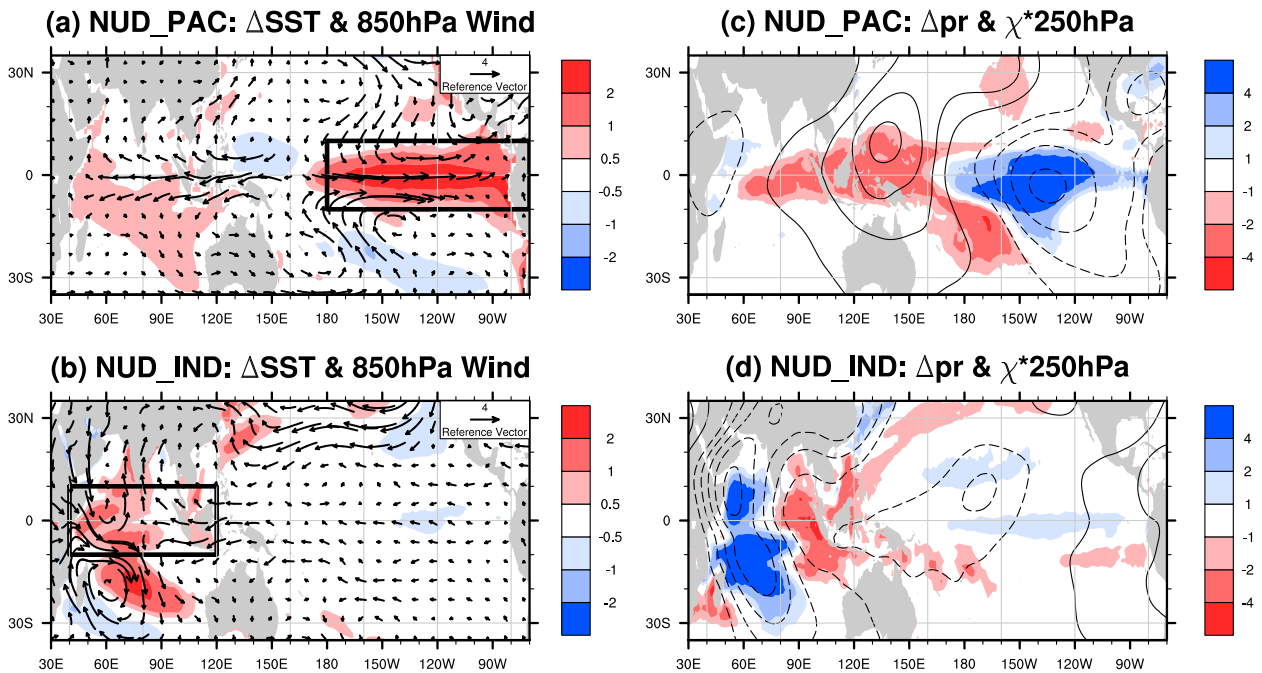


FIG. 6. As in Fig. 1, but for (top) NUD_{PAC} and (bottom) NUD_{IND} . (left) Black boxes indicate the nudging regions in each experiment. Note that a 20° -wide buffer zone extends on all sides of the nudging regions (not shown). In the buffer zone, the ocean temperatures and salinity are determined by a linear combination of nudging and the freely running ocean model, with the contribution from nudging decreasing to zero over the buffer zone as a Gaussian function of distance from the edge of the nudging region.

by construction. For this reason, we consider the nudging experiments to represent the separate canonical responses to ENSO and TIO forcing, independent of forcing from other basins.

The tropical SSTs in NUD_{PAC} , which we reiterate are freely coupled outside of the nudging region, reveal a strong ENSO-like pattern in the Pacific (which is imposed in the TEP through nudging) and weak basinwide warming of the TIO (Fig. 6a). The bulk of the warming in the TIO is a passive response to ENSO-induced subsidence and local reduction in cloudiness, leading to increased shortwave radiation at the surface with weak feedback onto the atmosphere circulation (Klein et al. 1999). In NUD_{IND} , the imposed SST pattern over the TIO projects onto the IOD (Fig. 6b) and is highly similar to that from the internally generated P_{nIa} (Fig. 1c). We find very little influence of the TIO on the Pacific in NUD_{IND} during DJF, with SSTs over the entire tropical Pacific showing neutral conditions or weak cooling. However, the SST in the TEP transitions to La Niña conditions during the following spring/summer (not shown), which is consistent with P_{nIa} (Fig. 5c) and the idea that the IOD exerts a lagged inverse influence over the Pacific (Izumo et al. 2010).

The tropical atmospheric response in NUD_{PAC} (Figs. 6a,b) displays the same pattern of ENSO-related

ascent, precipitation, and upper-tropospheric divergence over the Pacific seen in the P_{aI_n} case (Figs. 1b,e), but with roughly twice the amplitude (per unit tropical mean $|P'|$). The P_{aI_n} case provides the best comparison with NUD_{PAC} , because both represent the canonical ENSO signal (i.e., the atmospheric response independent of internally generated variability from the TIO or elsewhere in the tropics). In the case of NUD_{PAC} , the internally generated variability is removed by ensemble averaging, while in P_{aI_n} it is removed by design in the composite. The weaker atmospheric signals in P_{aI_n} are likely due to the composite being an average over a larger number of cases (84 winters versus 20 ensemble members) and the between-case variability in the composite being larger than the between-ensemble member variability in NUD_{PAC} (where each ensemble member received exactly the same boundary forcing).

The tropical atmospheric response in NUD_{IND} shows a strong dipole in precipitation over the TIO that indicates strong local convection and divergence over the western TIO (Fig. 6d). Overall, the tropical response in NUD_{IND} closely resembles the pattern in P_{nIa} (Fig. 1f); however, there are differences in the 850-hPa wind field. Convergence over the western TIO is mostly explained by anomalous easterlies across the Maritime Continent in P_{nIa} , while it is driven instead by

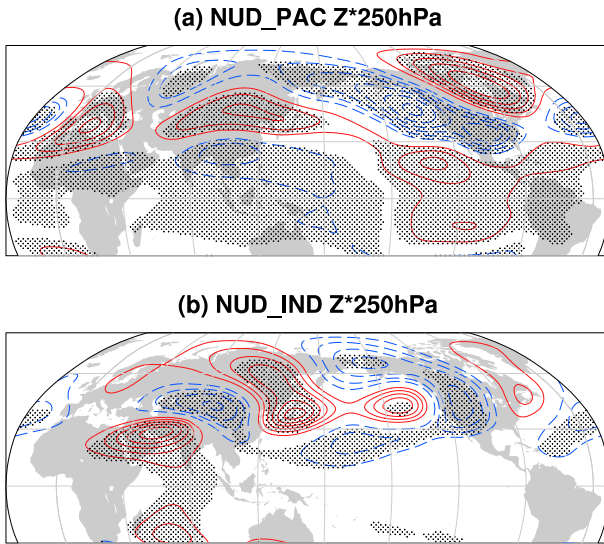


FIG. 7. As in Fig. 2, but for (top) NUD_{PAC} and (bottom) NUD_{IND} .

anomalous westerlies along the equator from the African coast in NUD_{IND} . The latter signal is also present in P_{nIa} but is secondary with respect to the eastern TIO changes. Similar anomalous cyclonic circulations straddling the equator around 60°E are found in both P_{nIa} and NUD_{IND} cases, with higher magnitude in the Southern Hemisphere in NUD_{IND} , corresponding to stronger imposed SSTs there within the buffer zone on the southern flank of the nudging region (Fig. 6b).

The Rossby wave source in each experiment is located on the poleward flank of the tropical convective anomaly: namely, $\sim 150^{\circ}\text{W}$ in NUD_{PAC} and $\sim 60^{\circ}\text{W}$ in NUD_{IND} . Given this longitudinal offset of the tropical responses, it is perhaps unsurprising that their extratropical wave fields are also very different. In NUD_{PAC} , the 250-hPa eddy geopotential height response (ΔZ^*250 ; Fig. 7a) resembles the P_{aIa} case (Fig. 2a), with a wave pattern over the North Pacific that projects onto the positive phase of the PNA. The anomaly correlation r_A between ΔZ^*250 in NUD_{PAC} and P_{aIa} in the Northern Hemisphere over the Indo-Pacific (20°E – 90°W) is $r_A = 0.60$. The wave response in NUD_{IND} (Fig. 7b) has very large amplitude (per unit tropical P') and does not resemble the pattern in P_{aIa} or P_{aIn} ($r_A = 0.20$ and -0.07 , respectively). Instead, it is broadly similar ($r_A = 0.51$) to the wave pattern in P_{nIa} (Fig. 2c), representing the wave teleconnection that originates from the TIO in the absence of competition from the Pacific.

b. Linear interference and the NAM response

Turning to the wave interference patterns, NUD_{PAC} produces weak constructive linear interference in wave 1 ($r_{\text{zp}} = 0.38$; Fig. 8a) and strong destructive interference

in wave 2 ($r_{\text{zp}} = -0.87$; Fig. 8b). This apparent cancellation between waves 1 and 2 results in a very weak (and not significant) negative NAM response in the polar stratosphere (Fig. 8c). In NUD_{IND} , there is very strong destructive interference in both waves 1 and 2 ($r_{\text{zp}} = -0.74$ and -0.90 , respectively; Figs. 8d,e), which drives a strong positive NAM response that is vertically coupled between the stratosphere and troposphere (Fig. 8f). Figures 8d–f are remarkably similar to those for the P_{nIa} case from piControl (Figs. 3g–i), implying that the NUD_{IND} experiment successfully isolates the TIO-induced teleconnection and NAM response.

The qualitative description of the role of linear interference provided by Fig. 8 can be better understood through the decomposition of the total eddy meridional heat flux v^*T^* , labeled TOTAL in Fig. 9 (see section 2d). Our results here are generally consistent with those derived from idealized modeling experiments in FK11 and FK13 and demonstrate that the NAM response is strongly related to the linear interference of $\Delta Z^*60^{\circ}\text{N}$ and Z^*_{clim} . The TOTAL term is opposite signed in NUD_{PAC} and NUD_{IND} , explaining the opposite-signed NAM responses, and its larger magnitude in NUD_{IND} partially explains the stronger NAM response in that case (although the relationship between TOTAL and the NAM response in the two experiments is clearly not linear).² In both experiments, $\text{EM} \gg \text{FL}$, which confirms that the quasi-stationary “forced” eddies in the EM dominate the wave driving of the NAM more than the eddies that are randomly phased between realizations (FL). The two nonlinear terms (EM_{NL} and FL) are inversely correlated, in agreement with FK13, implying that the randomly phased eddies act to partially damp the quasi-stationary eddies.

Interestingly, the sign and magnitude of the EM term in NUD_{IND} is dominated by EM_{LIN} , while in NUD_{PAC} , it is dominated by EM_{NL} . This is because EM_{LIN} is very weak in NUD_{PAC} because of strong cancellation of the positive wave-1 component by the negative wave-2 component. In addition, the relatively large contribution from EM_{NL} could be evidence that the forcing strength in NUD_{PAC} , which nudges toward SST anomalies that are stronger than any internally generated ENSO event (see section 2c), may represent too large of a perturbation, causing a breakdown of the linear decomposition where $\Delta v^* \geq v_c^*$ and/or $\Delta T^* \geq T_c^*$ (see section 2d). Overall, the sign and magnitude of TOTAL is strongly influenced by EM_{LIN} ; however, in the case of NUD_{PAC} , the TOTAL term is relatively weak because

² We emphasize that the heat flux decomposition is *not* scaled by the tropical $|P'|$.

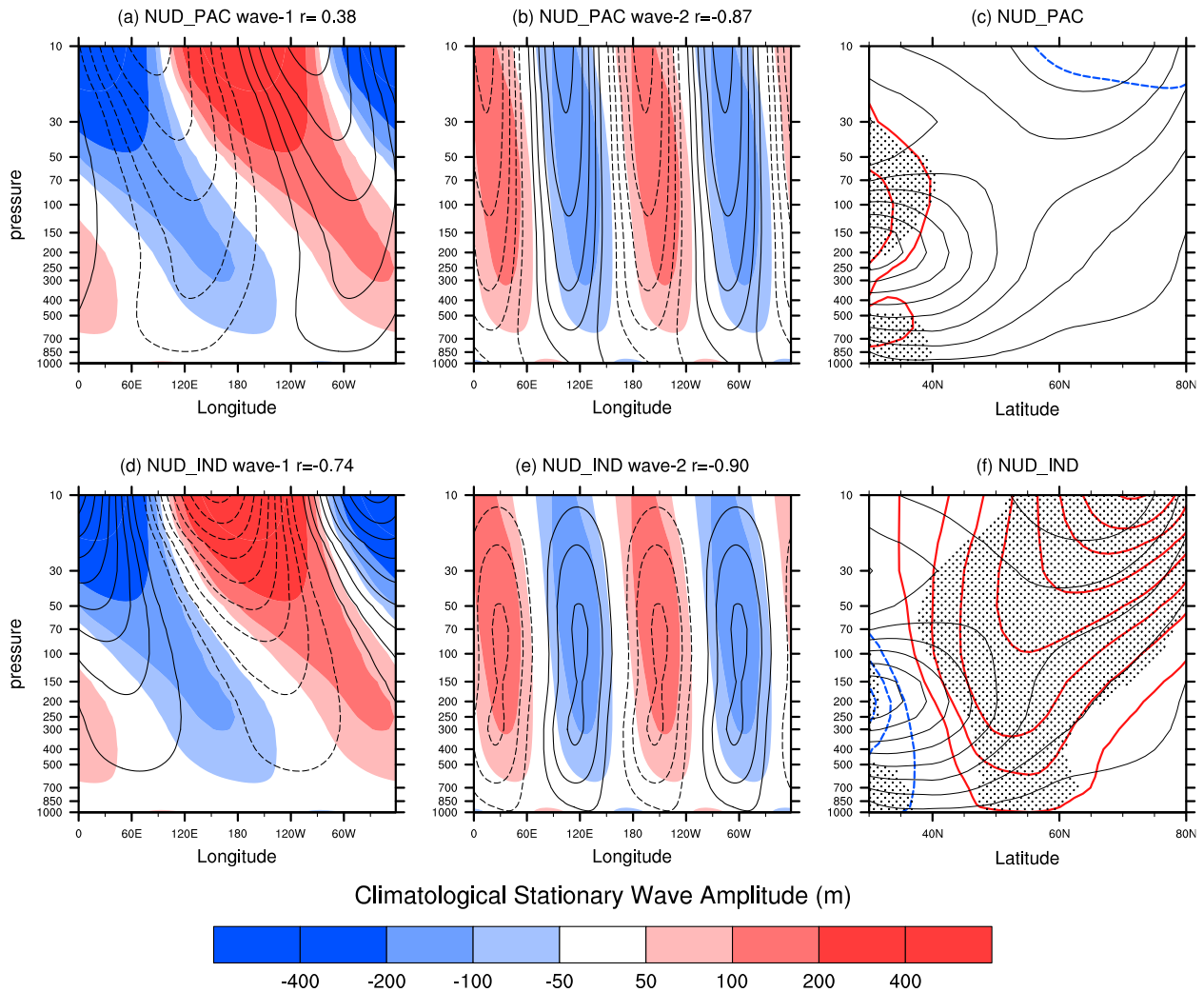


FIG. 8. As in Fig. 3, but for (top) NUD_{PAC} and (bottom) NUD_{IND}. Contour interval is 20 m for (left) wave 1 and 10 m for (center) wave 2, and it is 1 m s^{-1} for the (right) zonal wind.

of a small contribution from EM_{LIN} , a strong positive EM_{NL} , and a moderate offsetting contribution from FL.

Last, we turn to the intraseasonal variability in the NAM response and try to relate it to variations in the wave interference. The NUD_{PAC} case, with a positive-phase PNA teleconnection that closely resembles the internally generated response to ENSO in P_{aI_n} (c.f. Figs. 2b and 7a), produces a mostly negative NAM response, but it is weak and fluctuates in sign throughout the winter (Fig. 10a). The fluctuations are associated with intermittent shifts between constructive and destructive interference of the wave-1 and wave-2 components of EM_{LIN} (depicted by the r_{zp} values in the lower panel of Fig. 10a), and the peak negative NAM response in February–March coincides with a period of very strong constructive wave-1 linear interference. The NUD_{IND} response shows a strong and persistent

positive NAM signature initiated by strong destructive linear interference in waves 1 and 2 during December and maintained by consistent destructive interference in wave 2 throughout the winter (Fig. 10b). The wave-1 component returns to near neutral by February–March, which coincides with the termination of the NAM event in the stratosphere. Once again, the remarkable similarity between the response in NUD_{IND} and the P_{nI_a} case strongly supports our conclusion that teleconnections generated from the TIO that are independent of ENSO activity exert a profound influence on the northern extratropics.

5. Discussion and conclusions

The combination of analyses using the piControl composites (section 3) and nudging experiments (section 4)

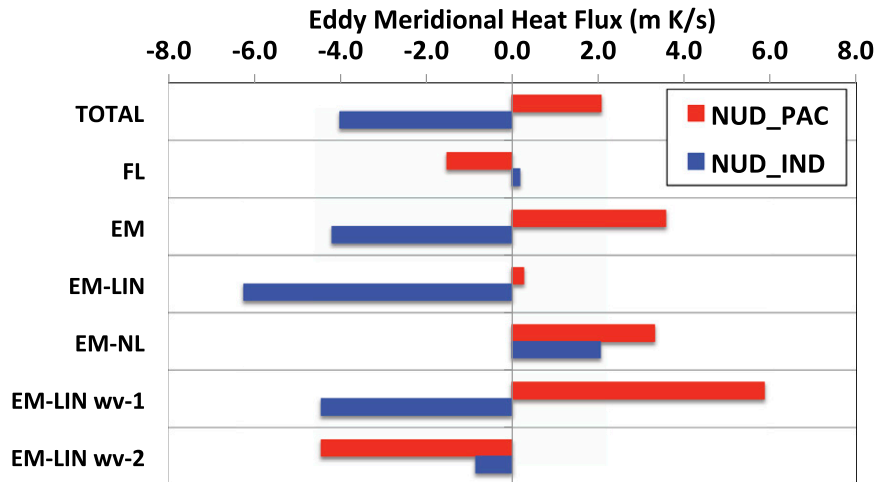


FIG. 9. (top) The contribution to the 100-hPa eddy meridional heat flux response ($\Delta\{v^*T^*\}$), averaged between 40° – 80° N, from the different terms in the decomposition described in section 2d. Red (blue) bars show the values for NUD_{PAC} (NUD_{IND}). Unlike the data in all other figures, the values in this figure have *not* been normalized by the amplitude of the tropical SST anomalies (see section 2d).

allows us to draw conclusions on the role of convective anomalies from the tropical Pacific and Indian Oceans in driving extratropical NAM responses. Increased precipitation in the central/eastern Pacific drives a negative NAM response, but, in agreement with Bell et al. (2009), it only emerges in late winter (February–March). When isolated from ENSO variability, increased precipitation over the western TIO drives a strong and persistent positive NAM response throughout the winter. These results agree broadly with other modeling studies highlighting the role of the TIO in driving teleconnections to the northern extratropics (Hoerling et al. 2004; Bader and Latif 2005; Annamalai et al. 2007). In addition, recent evidence from Molteni et al. (2015) demonstrates a similar role for the Indian Ocean in observations and hindcasts from a coupled seasonal forecast system. We reemphasize that, because models tend to overestimate the influence of the Pacific on TIO precipitation, it is likely that in nature a greater fraction of NAM variability may be explained by teleconnections associated with internal variability from the TIO (e.g., from IOD events).

Following on from FK11 and FK13, our principal message is that linear wave interference provides a useful dynamical framework for interpreting the opposite-signed NAM responses to Pacific and Indian Ocean forcing. The new angle presented here is that linear interference also appears to explain intraseasonal variability in the NAM responses. The P_{aI_n} and NUD_{PAC} cases both exemplify the canonical response to ENSO forcing in this model: that is, the response to Pacific forcing alone, without a significant contribution from

other regions in the tropics such as the Indian Ocean. The tropical, extratropical, and NAM responses in P_{aI_n} and NUD_{PAC} are highly similar, even though NUD_{PAC} is forced by ocean anomalies from the observed ENSO cycle 1997/98–1998/99 that have larger magnitudes than the model’s internally generated ENSO variability. The NAM response is significant and negative later in the winter (February–March; although in P_{aI_n} it is weakly negative in the troposphere throughout the winter), and this is related to constructive linear interference in wave 1. It is intriguing that P_{aI_n} and NUD_{PAC} both transition to negative NAM responses when the interference signatures in wave 1 and wave 2 are opposite (Figs. 4b and 10a). However, the wave-2 components are differently phased in the two cases: in P_{aI_n} , it transitions from constructive in November–December to destructive in February–March, while, in NUD_{PAC} , it is destructive throughout the winter. This is perhaps linked to the spatial pattern of tropical $\chi^*250\text{hPa}$ (Figs. 1e and 6c), which in P_{aI_n} evolves during February to more closely resemble NUD_{PAC} (not shown).

The P_{nI_a} and NUD_{IND} cases—characterized by active precipitation anomalies in the Indian Ocean that are independent of ENSO—show strong and persistent positive NAM responses, associated with strong destructive linear interference (Figs. 4c and 10b). These cases reveal important contributions to the NAM response from the wave-1 and wave-2 components, with some indication that the exceptional persistence of the positive NAM into late winter in the troposphere may be caused by the destructive interference in wave 2

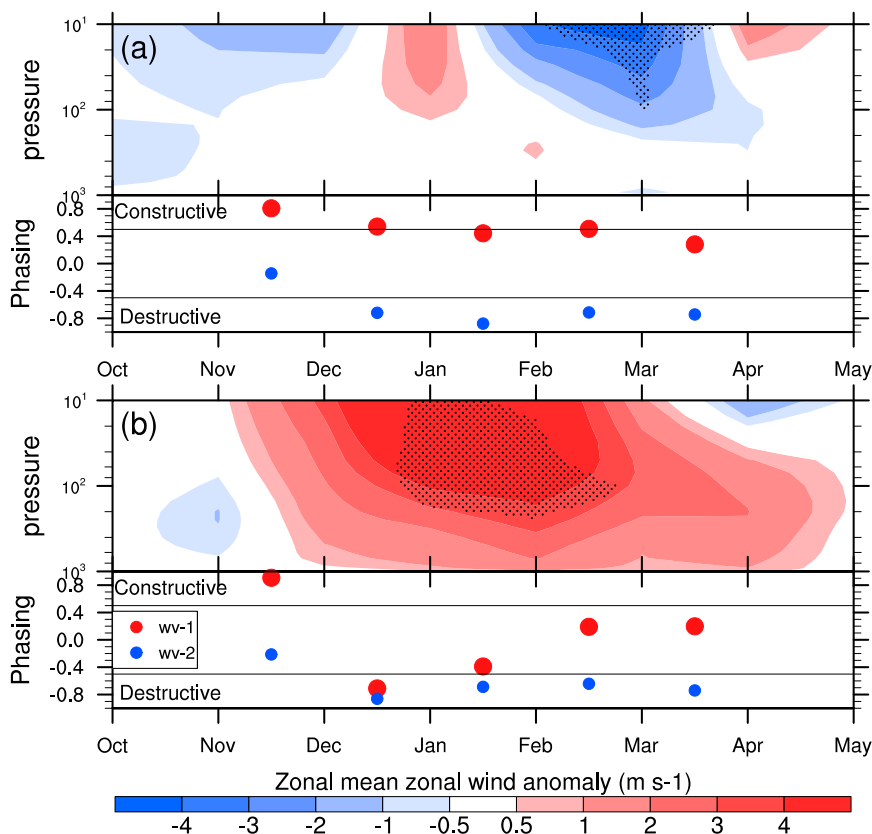


FIG. 10. As in Fig. 4, but for (top) NUD_{PAC} and (bottom) NUD_{IND} .

(in both cases, the wave-1 component moves into quadrature in February–March). The P_{aIa} case, where precipitation anomalies are active in both basins simultaneously, represents the canonical ENSO response plus a component of internal variability generated over the Indian Ocean. This case produces a very weak NAM response, which is associated with the interference patterns in waves 1 and 2 being mainly in quadrature (Fig. 4a).

Our results suggest a potential mechanism for intra-seasonal modulation of ENSO teleconnections through the Madden–Julian oscillation (MJO), since the MJO is associated with internally generated, large-amplitude precipitation events over the TIO. Cassou (2008) showed in reanalysis data that MJO phase 3–4 events (with convection centered over the TIO) tend to favor positive NAM circulation anomalies. Using the linear interference framework proposed above, we can predict that MJO phase 3–4 events occurring simultaneously with an ENSO event (i.e., peaking in DJF) could lead to cancellation and a weak NAM response. By contrast, either a weak MJO or phase 6–7 events (with convection suppressed over the TIO) would tend to amplify the background wave response to ENSO, which could lead

to an anomalously strong, and/or persistent, negative NAM response. This dynamical framework could also be applied in the context of climate change, in particular to interpreting the response of ENSO teleconnections to greenhouse gas forcing. For example, certain models participating in phase 5 of the Coupled Model Intercomparison Project (CMIP5), project a reinforcement and eastward shift of ENSO teleconnections in a warmer world, while other models show no change. In light of our results here and those of Fletcher and Minokhin (2015), who found substantial differences in the teleconnection and linear interference response of two models to imposed climate change, there appears to be a pressing need to examine inter-CMIP5 variability through the lens of modulation by the Indian Ocean and linear interference. Since part of the cause of differences between models is likely to lie in their parameterization of processes such as deep convection, such an analysis could focus on how improvements to model physics might reduce uncertainty in future projections.

Acknowledgments. CF acknowledges support from a Discovery Grant administered by the Natural Sciences and Engineering Research Council of Canada and the

generous financial, technical, and scientific support provided during his visit to CERFACS, Toulouse in late 2011. Financial support for CC has been provided by the EPIDOM/GICC and MORDICUS/ANR French national projects under Contact 10-MCGOT-GICC-7-CVS-131 and Contract ANR-13-SENV-0002-01. We are grateful to Dr. H. Annamalai and an anonymous reviewer for their comments that have helped to improve this manuscript.

REFERENCES

- Andrews, D. G., J. R. Holton, and C. B. Levoy, 1987: *Middle Atmosphere Dynamics*. International Geophysics Series, Vol. 40, Academic Press, 489 pp.
- Annamalai, H., P. Liu, and S.-P. Xie, 2005: Southwest Indian Ocean SST variability: Its local effect and remote influence on Asian monsoons. *J. Climate*, **18**, 4150–4167, doi:10.1175/JCLI3533.1.
- , H. Okajima, and M. Watanabe, 2007: Possible impact of the Indian Ocean SST on the Northern Hemisphere circulation during El Niño. *J. Climate*, **20**, 3164–3189, doi:10.1175/JCLI4156.1.
- Bader, J., and M. Latif, 2005: North Atlantic Oscillation response to anomalous Indian Ocean SST in a coupled GCM. *J. Climate*, **18**, 5382–5389, doi:10.1175/JCLI3577.1.
- Barsugli, J. J., and P. D. Sardeshmukh, 2002: Global atmospheric sensitivity to tropical SST anomalies throughout the Indo-Pacific basin. *J. Climate*, **15**, 3427–3442, doi:10.1175/1520-0442(2002)015<3427:GASTTS>2.0.CO;2.
- Bell, C. J., L. J. Gray, A. J. Charlton-Perez, M. M. Joshi, and A. A. Scaife, 2009: Stratospheric communication of El Niño teleconnections to European winter. *J. Climate*, **22**, 4083–4096, doi:10.1175/2009JCLI2717.1.
- Brönnimann, S., 2007: Impact of El Niño–Southern Oscillation on European climate. *Rev. Geophys.*, **45**, RG3003, doi:10.1029/2006RG000199.
- Butler, A. H., L. M. Polvani, and C. Deser, 2014: Separating the stratospheric and tropospheric pathways of El Niño–Southern Oscillation teleconnections. *Environ. Res. Lett.*, **9**, 024014, doi:10.1088/1748-9326/9/2/024014.
- Cagnazzo, C., and E. Manzini, 2009: Impact of the stratosphere on the winter tropospheric teleconnections between ENSO and the North Atlantic and European region. *J. Climate*, **22**, 1223–1238, doi:10.1175/2008JCLI2549.1.
- Cash, B. A., X. Rod, and J. L. Kinter, 2008: Links between tropical Pacific SST and cholera incidence in Bangladesh: Role of the eastern and central tropical Pacific. *J. Climate*, **21**, 4647–4663, doi:10.1175/2007JCLI2001.1.
- Cassou, C., 2008: Intraseasonal interaction between the Madden–Julian oscillation and the North Atlantic Oscillation. *Nature*, **455**, 523–527, doi:10.1038/nature07286.
- Charney, J. G., and P. G. Drazin, 1961: Propagation of planetary-scale disturbances from the lower into the upper atmosphere. *J. Geophys. Res.*, **66**, 83–109, doi:10.1029/JZ066i001p00083.
- Copsey, D., R. Sutton, and J. R. Knight, 2006: Recent trends in sea level pressure in the Indian Ocean region. *Geophys. Res. Lett.*, **33**, L19712, doi:10.1029/2006GL027175.
- Deser, C., and A. S. Phillips, 2006: Simulation of the 1976/77 climate transition over the North Pacific: Sensitivity to tropical forcing. *J. Climate*, **19**, 6170–6180, doi:10.1175/JCLI3963.1.
- Fletcher, C. G., and P. J. Kushner, 2011: The role of linear interference in the annular mode response to tropical SST forcing. *J. Climate*, **24**, 778–794, doi:10.1175/2010JCLI3735.1.
- , and —, 2013: Linear interference and the Northern Annular Mode response to tropical SST forcing: Sensitivity to model configuration. *J. Geophys. Res.*, **118**, 4267–4279, doi:10.1002/jgrd.50385.
- , and I. Minokhin, 2015: Linear interference and the northern annular mode response to El Niño and climate change. *Climate Dyn.*, doi:10.1007/s00382-015-2518-0.
- Free, M., and D. J. Seidel, 2009: Observed El Niño–Southern Oscillation temperature signal in the stratosphere. *J. Geophys. Res.*, **114**, D23108, doi:10.1029/2009JD012420.
- Garfinkel, C. I., and D. L. Hartmann, 2008: Different ENSO teleconnections and their effects on the stratospheric polar vortex. *J. Geophys. Res.*, **113**, D18114, doi:10.1029/2008JD009920.
- Guo, F., Q. Liu, S. Sun, and J. Yang, 2015: Three types of Indian Ocean dipoles. *J. Climate*, **28**, 3073–3092, doi:10.1175/JCLI-D-14-00507.1.
- Hoerling, M. P., J. W. Hurrell, T. Xu, G. T. Bates, and A. S. Phillips, 2004: Twentieth century North Atlantic climate change. Part II: Understanding the effect of Indian Ocean warming. *Climate Dyn.*, **23**, 391–405, doi:10.1007/s00382-004-0433-x.
- Ineson, S., and A. A. Scaife, 2009: The role of the stratosphere in the European climate response to El Niño. *Nat. Geosci.*, **2**, 32–36, doi:10.1038/ngeo381.
- Izumo, T., and Coauthors, 2010: Influence of the state of the Indian Ocean dipole on the following year’s El Niño. *Nat. Geosci.*, **3**, 168–172, doi:10.1038/ngeo760.
- Kim, B.-M., S.-W. Son, S.-K. Min, J.-H. Jeong, S.-J. Kim, X. Zhang, T. Shim, and J.-H. Yoon, 2014: Weakening of the stratospheric polar vortex by Arctic sea-ice loss. *Nat. Commun.*, **5**, 4646, doi:10.1038/ncomms5646.
- Klein, S. A., B. J. Soden, and N.-C. Lau, 1999: Remote sea surface temperature variations during ENSO: Evidence for a tropical atmospheric bridge. *J. Climate*, **12**, 917–932, doi:10.1175/1520-0442(1999)012<0917:RSSTVD>2.0.CO;2.
- Madec, G., 2008: NEMO ocean engine. Institut Pierre-Simon Laplace (IPSL) Tech. Note 27, 367 pp. [Available online at http://www.nemo-ocean.eu/content/download/21612/97924/file/NEMO_book_3_4.pdf.]
- Molteni, F., T. N. Stockdale, and F. Vitart, 2015: Understanding and modelling extra-tropical teleconnections with the Indo-Pacific region during the northern winter. *Climate Dyn.*, doi:10.1007/s00382-015-2528-y.
- Morgensen, K., M. Balmaseda, A. Weaver, M. Martin, and A. Vidard, 2009: NEMOVAR: A variational data assimilation system for the NEMO ocean model. *ECMWF Newsletter*, No. 120, ECMWF, Reading, United Kingdom, 17–21.
- Nishii, K., H. Nakamura, and Y. J. Orsolini, 2011: Geographical dependence observed in blocking high influence on the stratospheric variability through enhancement and suppression of upward planetary-wave propagation. *J. Climate*, **24**, 6408–6423, doi:10.1175/JCLI-D-10-05021.1.
- Randel, W. J., R. R. Garcia, N. Calvo, and D. Marsh, 2009: ENSO influence on zonal mean temperature and ozone in the tropical lower stratosphere. *Geophys. Res. Lett.*, **36**, L15822, doi:10.1029/2009GL039343.
- Rayner, N. A., D. E. Parker, E. B. Horton, C. K. Folland, L. K. Alexander, and D. P. Rowell, 2003: Global analyses of sea surface temperature, sea ice and night marine air temperature since the late nineteenth century. *J. Geophys. Res.*, **108**, 4407, doi:10.1029/2002JD002670.
- Ruprich-Robert, Y., and C. Cassou, 2014: Combined influences of seasonal East Atlantic Pattern and North Atlantic Oscillation to excite Atlantic multidecadal variability in a climate model. *Climate Dyn.*, **44**, 229–253, doi:10.1007/s00382-014-2176-7.

- Saji, N. H., B. N. Goswami, P. N. Vinayachandran, and T. Yamagata, 1999: A dipole mode in the tropical Indian Ocean. *Nature*, **401**, 360–363. [Available online at <http://www.nature.com/nature/journal/v401/n6751/abs/401360a0.html>.]
- Sanchez-Gomez, E., C. Cassou, Y. Ruprich-Robert, E. Fernandez, and L. Terray, 2015: Drift dynamics in a coupled model initialized for decadal forecasts. *Climate Dyn.*, doi:10.1007/s00382-015-2678-y.
- Smith, K. L., C. G. Fletcher, and P. J. Kushner, 2010: The role of linear interference in the annular mode response to extratropical surface forcing. *J. Climate*, **23**, 6036–6050, doi:10.1175/2010JCLI3606.1.
- Taguchi, M., and D. L. Hartmann, 2006: Increased occurrence of stratospheric sudden warmings during El Niño as simulated by WACCM. *J. Climate*, **19**, 324–332, doi:10.1175/JCLI3655.1.
- Thompson, D. W. J., and J. M. Wallace, 2000: Annular modes in the extratropical circulation. Part I: Month-to-month variability. *J. Climate*, **13**, 1000–1016, doi:10.1175/1520-0442(2000)013<1000:AMITEC>2.0.CO;2.
- Ting, M., M. P. Hoerling, T. Xu, and A. Kumar, 1996: Northern Hemisphere teleconnection patterns during extreme phases of the zonal-mean circulation. *J. Climate*, **9**, 2614–2633, doi:10.1175/1520-0442(1996)009<2614:NHTPDE>2.0.CO;2.
- Trenberth, K. E., J. M. Caron, D. P. Stepaniak, and S. Worley, 2002: Evolution of El Niño–Southern Oscillation and global atmospheric surface temperatures. *J. Geophys. Res.*, **107**, AAC 4-1–AAC 4-15, doi:10.1029/2000JD000298.
- Voldoire, A., and Coauthors, 2013: The CNRM-CM5.1 global climate model: Description and basic evaluation. *Climate Dyn.*, **40**, 2091–2121, doi:10.1007/s00382-011-1259-y.